Florence, Italy 12-16 July 2015
ICSV22
The 22nd International Congress on Sound and Vibration

IMPLEMENTING THE FFOWCS WILLIAMS AND HAWKINGS ACOUSTIC ANALOGY IN ANTARES

Danilo Di Stefano, Aldo Rona, Edward Hall
Department of Engineering, University of Leicester, University Road, LE1 7RH, Leicester, England
email: dds13@leicester.ac.uk

Guillaume Puigt
CERFACS, 42, av. Coriolis, 31057, Toulouse, Cedex, France

The aerodynamic noise radiating from an unsteady flow can be extracted by an acoustic analogy approach from time-resolved Computational Fluid Dynamic (CFD) simulations. For this purpose, a Ffowcs Williams and Hawkings (FW-H) post-processor is developed, based on an advanced time formulation. The method is coded in Python and embedded in Antares, which is a CFD companion software developed by Cerfacs, France. The availability in Antares of input and output data interfaces for structured and unstructured CFD geometries and solutions provides a good software development platform. The new post-processor is tested on a hierarchy of noise sources of increasing complexity, for which comparison is made with existing data. The radiating field from a simple monopole is considered first, with progression to a subsonic jet test case, for which acoustic data have been estimated by Bogey and Bailly (2006). CFD results obtained at Cerfacs (France), using a compressible Large Eddy Simulation (LES) on the same test case, provide the input to the acoustic analogy to estimate the far-field noise. The far-field noise predictions are compared to the acoustic results obtained with the CFD software elsA (Onera, France), that uses the same Ffowcs Williams and Hawkings acoustic analogy formulation and these are found in good agreement.

1. Introduction

The noise generated by unsteady flows can be predicted by different approaches, such as direct Computational Aeroacoustics (CAA), a boundary element integral method, or by acoustic analogy. Using an acoustic analogy approach, the CFD and CAA solvers can be written independently from one another. The CAA solver acts as a "black box", receiving at each acoustic time-step an input from the CFD solver and evaluating its contribution to the acoustic pressure at specified observer positions. The input from the CFD consists of the unsteady hydrodynamic flow field in terms of density, pressure and velocity. The other inputs required by the CAA solver are the Ffowcs Williams and Hawkings (FW-H) integration surface topology (Section 2) and the position of the acoustic observer with respect to the flow. From these data, the CAA solver can compute its output, that is, the acoustic pressure fluctuation at the observer position. This process is repeated at each time-step to build up a pressure time history at the observer position, which is then stored. By splitting the generation of the flow field data from the evaluation of the acoustic pressure at the observer position, a more general CAA tool is

obtained, which can then be linked to different CFD software. This tool reduces the complex task of coding a full computational aeroacoustic scheme to developing a simpler data structure interface, so that custom CFD output can be read by the CAA post-processor.

The focus of this paper is the development of a FW-H post-processor as a plug-in tool instead of being embedded in a CFD code suite, following the above stated approach. The implementation of the FW-H acoustic analogy in the advanced time formulation [1] described by Casalino [2] is coded in Python and embedded in Antares 1.4.0 [3]. Antares is a software package containing pre- and post-processing libraries and numerical flow visualization tools, for the purpose of performing steady and unsteady flow analysis both a-posteriori and in real time. The availability in Antares of input and output data interfaces for popular structured and unstructured CFD geometries and solutions provides a good starting point for developing a FW-H post-processor of wide access and usability.

The aim is to build a numerical tool that is accessible to the wider research community to use, develop, and improve. The way the FW-H tool is implemented reflects this community goal. The development of Antares is coordinated by Cerfacs, France, with the aim of supporting the CFD and the aeroacoustic communities. The FW-H post-processor is expected to be adopted and improved, from a computing performance viewpoint, by the Cerfacs software coordination team, ensuring its integrity and reliability for the benefit of all the researchers in this field.

The new FW-H tool is coded in Python 2.7.9 and a validation process is implemented. For this purpose, a series of tests of increasing complexity is carried out, building towards comparing the predictions with the ones from the elsA CFD solver [4] by Onera, France, in Section 4.3. This solver contains the same acoustic analogy formulation the authors are implementing in Antares, which provides an opportunity for verifying the implementation of the advanced time algorithm on the same CFD data set. Specifically, the new post-processor is applied to a single jet test case by Bogey and Bailly [5], for which CFD results by LES are obtained at Cerfacs using elsA. Far-field noise data are estimated from the CFD database and the predictions are then compared with the ones available from elsA run on the same test case. This process aims to verify the correct implementation of the advanced time algorithm and to give confidence in the new numerical tool for estimating near-field and far-field noise by acoustic analogy.

2. The Ffowcs Williams and Hawkings acoustic analogy

Lighthill [6] developed an exact rearrangement of the Navier-Stokes equations obtaining an inhomogeneous wave equation with a non-linear right-hand side. The resulting equation recasts acoustic density fluctuations generated in a turbulent flow as if propagating in a uniform medium at rest. This medium is the acoustic analogy to the non-uniform turbulent flow. From the seminal work of Lighthill, more generally applicable acoustic analogy formulations have been developed. The integral solution reported by Casalino [2] to the FW-H equation [7] is a generalization of the Lighthill acoustic analogy for flows including bodies in arbitrary motion. In this generalization, which follows the same principles of the FW-H analogy, the fluid is unbounded but partitioned into regions by a closed surface [7], as sketched in Fig. 1(a). This surface does not need to coincide with a physical body and can be permeable [8, 9]. The surface requirements are discussed in details by Brentner and Farassat [8].

The flow outside this surface is modelled by the Navier-Stokes equations. Inside the closed surface, the conservation laws are assumed not to apply and the flow state is specified arbitrarily. In order to maintain the discontinuity generated in such a way across the surface, mass and momentum sources are distributed over the closed integration surface [7]. This process is carried out from the time-resolved estimates of pressure, density and velocity on the FW-H integration surface, obtained independently by CFD.

The equations of conservation of mass and momentum are taken as valid everywhere in an exterior flow domain free from solid boundaries. The theory of generalized functions is used to combine these equations in the form of an inhomogeneous wave equation. This embedding procedure is detailed by

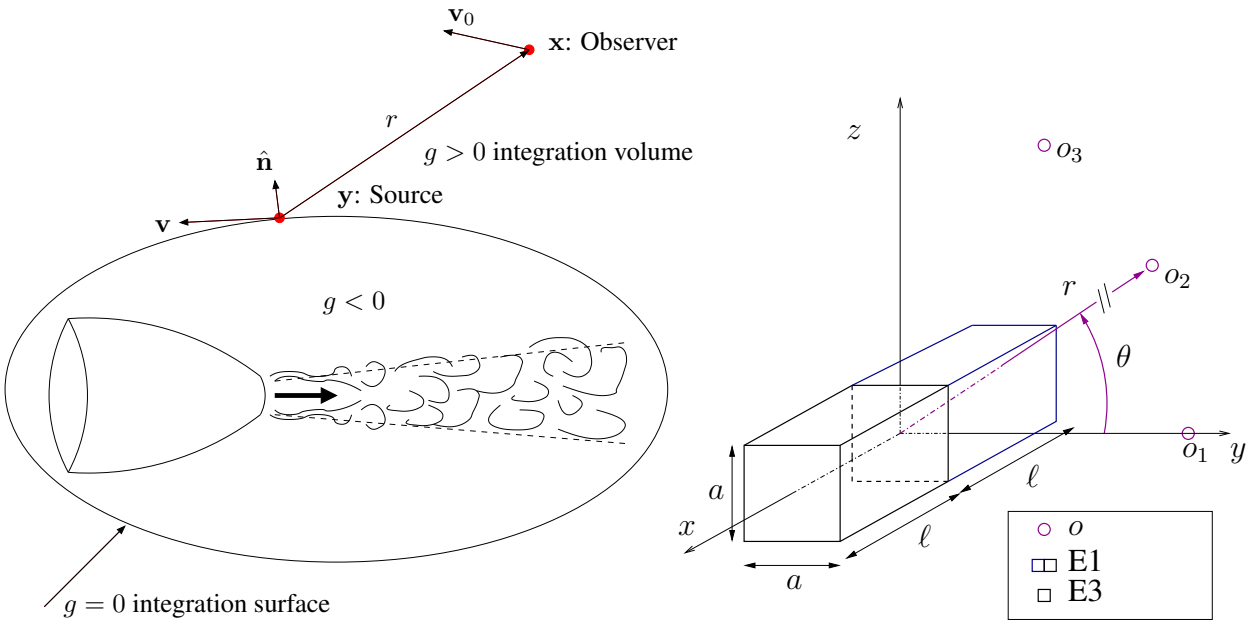

(a) Radiation in an unbounded flow (b) Prismatic integration surface

Figure 1: Schematic of Ffowcs Williams and Hawkings surfaces.

Farassat [10] and only a brief outline is given herein for conciseness.

Let $g(\mathbf{x}, t) = 0$ be the equation describing the moving control surface of Fig. 1(a), whose points move at velocity $\mathbf{v}(\mathbf{x}, t)$ [2]. g is defined to satisfy the property $\nabla g = \hat{\mathbf{n}}$ on the surface, where $\hat{\mathbf{n}}$ is the outward pointing unit normal vector. Following this procedure, the flow is partitioned into three regions according to the value of g, as shown in Fig. 1(a). A point enclosed by the integration surface satisfies $g < 0$ and this flow field portion can be replaced by a quiescent fluid. Mass and momentum sources are then distributed on the surface $g(\mathbf{x}, t) = 0$, which allows the conservation laws across $g(\mathbf{x}, t) = 0$ to be satisfied.

The mass and momentum conservation equations are recast to obtain the FW-H equation

$$\Box^2\{(\rho - \rho_0)\, c^2 H(g)\} = \frac{\partial^2\{T_{ij} H(g)\}}{\partial x_i \partial x_j} - \frac{\partial\{L_i \delta(g)\}}{\partial x_i} + \frac{\partial\{Q\delta(g)\}}{\partial t}\ , \tag{1}$$

where $H(g)$ is the Heaviside function and in the first source term on the right-hand side T_{ij} is the Lighthill stress tensor [6]. The second and third contributions are, respectively, the surface source distributions of momentum and mass. Expressions for these source terms are given in Ffowcs Williams and Hawkings [7].

Casalino [2] reports the integral solution of the FW-H equation in the advanced time formulation. In this solution, the acoustic pressure fluctuation $p' = p - p_0$ perceived by an observer located at the vector position $\mathbf{x}$ at time t is given by:

$$p'(\mathbf{x}, t) = p'_Q(\mathbf{x}, t) + p'_L(\mathbf{x}, t) + p'_T(\mathbf{x}, t)\ , \tag{2}$$

where subscripts Q, L, and T are, respectively, the quadrupole, loading, and thickness noise contributions to p' from the source field located at $\mathbf{y}$ generated at retarded time $\tau_{ret} = t - c^{-1}\,|\mathbf{x} - \mathbf{y}\,(\tau_{ret})|$. τ_{ret} accounts for the time of flight of the noise propagating from $\mathbf{y}$ to $\mathbf{x}$ at the constant speed of sound c. Expressions for these contributions are given in Casalino [2].

3. Implementation in Antares

A discretized form of Eq. (2) is implemented in Antares. The quadrupole source term is neglected in this first implementation, with the aim to reproduce exactly the formulation of the elsA FW-H

solver. In this way, a direct comparison between the acoustic predictions from the two codes can be performed. Moreover, it is often possible in CAA to neglect the volume source distribution of T_{ij}, primarily due to the quadrupole term representing the smallest contribution to noise radiation at low Mach numbers. One further advantage of this approach is the considerable decrease in the computational cost of the simulation, by reducing a three-dimensional numerical integration to a two-dimensional one.

In this first implementation, the post-processor is to be used with structured computational meshes, which are used in many CFD codes. According to this CFD mesh topology, the FW-H surface $g(\mathbf{x}, t) = 0$ is partitioned into different zones coinciding with different mesh blocks. The intersection between $g(\mathbf{x}, t) = 0$ and the CFD mesh determines the set S_j of cell faces lying on the FW-H surface. For each S_j, the post-processor estimates the contribution to p' at the observer position.

The FW-H algorithm is structured in the following way: At each discrete acoustic time τ^n, a loop over the observer positions $\mathbf{x}_i$ is performed. For each $\mathbf{x}_i$, the contribution from the FW-H surface is estimated, by looping over the S_js. For each S_j, a loop is then performed over the surface elements dS_k of S_j, on which the discretized form of the L and T terms is evaluated. For each dS_k, the advanced time is also estimated from the retarded time equation [2] in order to save the p' contribution at the correct observer time.

This process is then repeated at different discrete acoustic times τ^n. Advancing in time, a pressure fluctuation history is reconstructed and the final output of the tool is a matrix storing, for each observer position, the pressure fluctuation $p'(\mathbf{x}_i, t)$ as a discretised time array.

For each discrete acoustic time τ^n, the acoustic analogy post-processor reads the CFD solution and retains the flow field data relative to the previous iteration τ^{n-1}. This enables the estimation of the source time derivatives using the backward finite difference approximation

$$\dot{z} = \frac{\partial z}{\partial \tau} \approx \frac{(z^n - z^{n-1})}{\Delta \tau} \ , \tag{3}$$

where z is a source term variable.

Considering the different characteristic time and length scales between the hydrodynamic and the acoustic fields, the acoustic simulation usually requires a lower resolution in time. For this reason, the new tool is designed such that it can perform the numerical integration every m CFD time-steps. For the jet test case from Bogey and Bailly, the relationship between the acoustic and the CFD time-steps is

$$\Delta \tau_{ac} = 10 \times \Delta \tau_{CFD} \ . \tag{4}$$

This choice allows the CAA simulation to use less computer time and memory.

4. Results and Discussion

The implementation of the advanced time formulation of the FW-H acoustic analogy approach of Section 3 is tested on noise source fields of increasing complexity in Sections 4.1-4.3. All tests use FW-H integration surfaces of the same topology, as sketched in Fig. 1(b). A square prism of cross-section $a \times a$, centred at the origin, encloses the noise sources. In the first and second tests, respectively, a monopole and a dipole are located at the origin and the height of the FW-H prism extends symmetrically about the source over the range $-\ell \leq x \leq \ell$, as per configuration E1 in Fig. 1(b). In the last test, the FW-H prism extends over the range $0 \leq x \leq \ell$, giving configuration E3 in Fig. 1(b). All tests use the same circular array of three far-field observers (o_1, o_2, o_3) located on the $y - z$ plane at radial distance r from the origin and at the azimuthal angle θ of $(0, \pi/5, 2\pi/5)$ from the y axis.

4.1 Monopole

A monopole of acoustic power $W = 96.83$ dB re 1pW located at the origin radiates at a frequency $f = 42.5$ Hz. This acoustic power gives a Sound Pressure Level (SPL) of 80 dB re 20μPa at 2 m from the source. Far-field noise predictions are obtained at $r = 0.6$ m and $r = 1.2$ m on the circular array of Fig. 1(b) from the application of the acoustic analogy of Section 3. The FW-H surface is used in configuration $E1$ with $a = 0.12$ m and $\ell = 0.06$ m. Figure 2(a) displays the predicted acoustic pressure fluctuation p' versus the benchmark analytical result $p' = B\sin(\omega t - kr)$, where $B = -\rho_0 c_0 q k (4\pi r)^{-1}$, $\rho_0 = 1.225$ kg/m^3, $c_0 = 340.25$ m/s, $k = \omega/c_0$, $q = \left(8\pi c_0 W \rho_0^{-1}\omega^{-2}\right)^{1/2}$ and $\omega = 2\pi f$. The reference analytical solution is labelled 'ref' in Fig. 2. The results show that the FW-H post-processor matches the analytical pressure fluctuation in amplitude, phase and frequency at both radial distances. A small phase shift is present in the numerical solution. This is not noticeable from Fig. 2(a), because the order of magnitude of this phase shift is $\Delta\tau/2$. It is suspected that this difference is due to the backward finite difference approximation of Eq. (3) used to discretize the source time derivatives.

The ratio of the peak to peak pressure fluctuation amplitude at $r = 0.6$ m and $r = 1.2$ m for both numerical and analytical predictions is 2.0, showing that the FW-H method correctly predicts the geometric scaling of the acoustic intensity with increasing radial distance. The spherically symmetric radiation pattern of the monopole is correctly captured by the FW-H method, with the acoustic pressure fluctuation amplitude at o_2 and o_3 being 0.99981 and 0.99974 of that at o_1, with no appreciable difference in phase and frequency.

The effect of the spatial discretization error of the FW-H surface on the numerical predictions is investigated by varying the number of dS_k discrete faces on the FW-H surface from 6×20^2 to 6×40^2 and to 6×80^2. In this analysis, the time step is kept constant to a very small value, $\Delta\tau = 1.378\times10^{-6}$ s, in order to reduce as much as possible the error contribution due to the temporal discretization. The error in the fluctuating pressure amplitude between the numerical and the analytical solutions at o_1 at $r = 0.6$ m reduces from 0.1122% in the baseline mesh to 0.0243% and 0.0024%, respectively on the 6×40^2 and 6×80^2 meshes. No appreciable difference in frequency is observed. The effect of the temporal discretization error is also examined by increasing the temporal resolution from $\Delta\tau = 8.820\times10^{-5}$ s to $\Delta\tau = 4.410\times10^{-5}$ s and to $\Delta\tau = 2.205\times10^{-5}$ s, resulting in a decrease of the error in the fluctuating pressure amplitude from 2.7198% to 0.7690% and to 0.2273% at the same observer location. In this case, the mesh is refined to 6×160^2 in order to reduce the error contribution due to the spatial discretization. In both analyses, the reference analytical fluctuating pressure amplitude is B evaluated at $r = 0.6$ m. Thus, as both the spatial and temporal resolutions are improved, the numerical solution converges to the analytical one. The spatial and temporal resolutions of 100 points per wavelength (6×20^2 dS_k discrete faces) and 40 points per period ($\Delta\tau = 4.41\times10^{-5}$ s) appear appropriate for this application.

4.2 Dipole

In the second test, a y-axis dipole sound source is tested with the same FW-H integration surface and microphone array as Section 4.1. The dipole strength is defined to obtain the same 80 dB re 20μPa on the y axis, 2 m away from the source. The acoustic pressure fluctuation predicted at o_1 at $r = 0.6$ m is shown in Fig. 2(b) together with the reference analytical solution

$$p' = B\frac{k(\mathbf{r}\cdot\mathbf{d})}{r}\left[\cos(\omega t - kr) + \frac{\sin(\omega t - kr)}{kr}\right]. \tag{5}$$

There is no noticeable difference in amplitude, phase and frequency between the two time traces, indicating that the sound pressure is correctly predicted by the FW-H method. The same small phase shift is found as in Section 4.1. Doubling the distance to the observer to $r = 1.2$ m reduces the pressure perturbation amplitude by a factor of 0.495 in both the analytical and the numerical results,

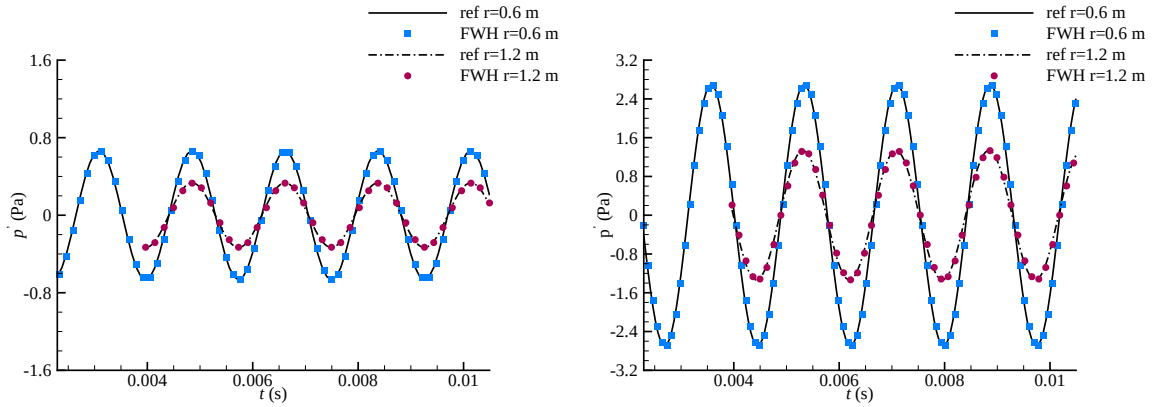

(a) Monopole (b) Dipole at $\theta = 0$

Figure 2: Sound pressure fluctuation at increasing radial distance r. Observer o_1.

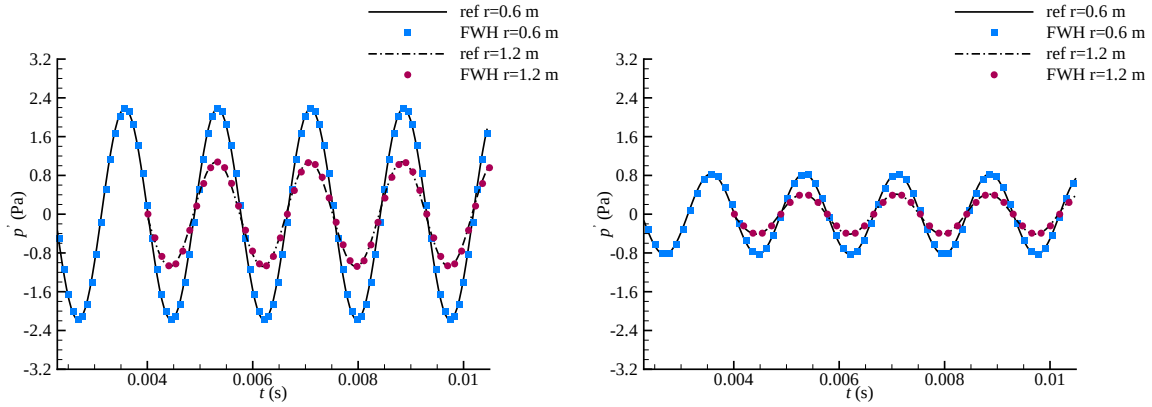

(a) Observer o_2 at $\theta = \pi/5$ (b) Observer o_3 at $\theta = 2\pi/5$

Figure 3: Sound pressure fluctuation at increasing radial distance r from a dipole.

confirming that the analytical scaling of the sound intensity with distance from the sound source is correctly captured. The match in amplitude, phase and frequency between the reference analytical pressure fluctuation and the FW-H integration surface method is maintained at this increased radial distance. Figures 3(a) and 3(b) display, respectively, the acoustic pressure fluctuation at increasing azimuthal angles from the dipole axis. The pressure time traces display the same characteristics as the FW-H predictions along the axis in that they match the reference solution in amplitude, phase and frequency. The predictions confirm that the FW-H method reproduces the correct analytical scaling of the acoustic pressure fluctuation with increasing r off-axis, with the ratio of the acoustic pressure amplitudes at $r = 1.2$ m and $r = 0.6$ m at $\theta = \pi/5$ being 0.495.

The dipole test case enables the assessment of the performance of the FW-H method in capturing the radiation characteristics of a directive source. The directivity of this sound source is $D(\theta) = \cos(\theta)$ on the $y - z$ plane. From Figs. 3(a) and 2(b), the ratio of the acoustic pressure amplitude at $\theta = \pi/5$ and $\theta = 0$, at $r = 0.6$ m, is 0.8085 against $\cos(\pi/5) = 0.8090$. From Figs. 3(b) and 2(b), the corresponding ratio is 0.3086 against $\cos(2\pi/5) = 0.3090$. This indicates that the FW-H procedure is able to capture the radiation characteristics of directive sources to a good approximation.

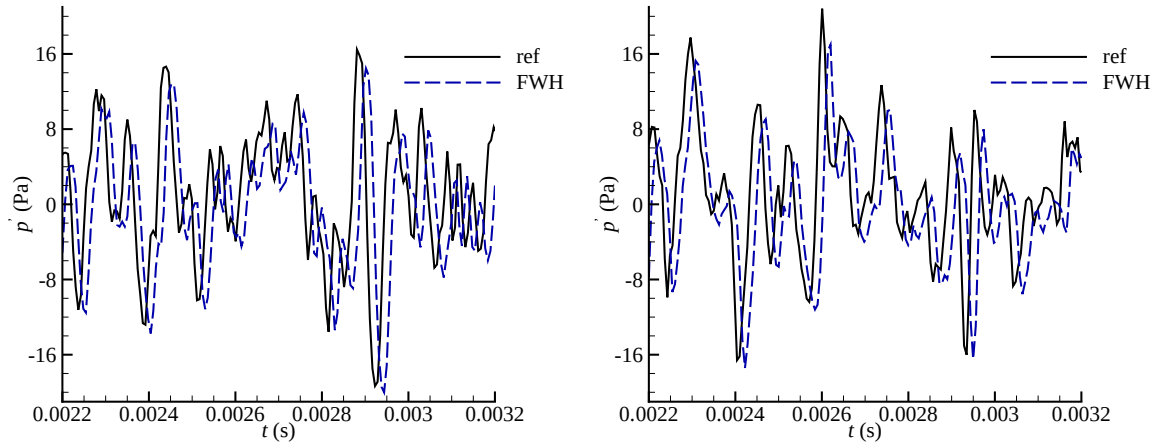

(a) Observer o_1 at $\theta = 0$

(b) Observer o_2 at $\theta = \pi/5$

Figure 4: Sound pressure fluctuation from a Mach 0.9 jet.

4.3 Jet

The FW-H method of Section 3 is used to estimate the aerodynamic noise from an isothermal circular jet [5] modelled at a nozzle exit Mach number of 0.9 and at a Reynolds number of 4×10^5. Estimates of the unsteady flow field are obtained from an archived Large Eddy Simulation (LES) provided by Cerfacs, extracted at the Ffowcs Williams and Hawkings surface of configuration E3, Fig. 1(b). The jet axis coincides with the x-axis and the nozzle outflow is in the positive x direction. The FW-H surface base length a is 6 jet diameters (D_e) and the FW-H surface axial length ℓ is $12.5D_e$. The acoustic pressure fluctuation is estimated at the constant radial distance $r = 30D_e$ at $\theta = 0$ and $\theta = \pi/5$ (o_1 and o_2 in Fig. 1(b)). The contributions from the square faces at $x = 0$ and $x = \ell$ are significantly affected by the hydrodynamic field of the jet crossing these surfaces and have therefore been excluded from the integration procedure. The same 'open surface' FW-H integration was carried out using the elsA software, from Onera, on the same data set. Figure 4(a) shows the acoustic pressure fluctuation estimated using the current FW-H implementation versus the reference prediction from elsA, denoted by 'ref' in Fig. 4. The acoustic pressure fluctuation at the observer o_1 is broadband and non-periodic, as shown by the superimposition of large and small amplitude pressure oscillations in Fig. 4(a). This results in a complex pressure perturbation trend. The current implementation of the FW-H method appears to follow this trend well, with a small phase lead and a small negative mean pressure offset to the reference solution. A similar match is obtained at the off-axis observer position o_2, shown in Fig. 4(b). This indicates that the current implementation reproduces consistently the frequency content and the directivity characteristics of the reference FW-H prediction from elsA.

5. Conclusions

Progress has been made towards validating the output from a Ffwocs Williams and Hawkings post-processor designed as a plug-in tool instead of being embedded in a CFD code suite. It is expected that the availability of the new post-processor will be of benefit to the aeroacoustic community. Past examples of software shared by many users have demonstrated the considerable benefits that this approach can give to the scientific community. These include software affordability, concerted code debugging and improvement, continuous software validation and verification in the community, and implementation and testing of the latest algorithms on an accessible platform. The knowledge and

technology sharing approach adopted for this work will enable, over time, the production of state of the art software, with good longevity and reliability.

6. Acknowledgments

The dissemination of these results has received funding from the European Union Seventh Framework Programme FP7/2007-2013 under grant agreement no. 317142.

REFERENCES

1. Rona, A., Aerodynamic and aeroacoustic estimations of oscillatory supersonic flows, Ph.D. thesis, *Department of Aeronautics and Astronautics, University of Southampton, UK*, (1997).

2. Casalino, D., An advanced time approach for acoustic analogy predictions, *Journal of Sound and Vibration*, **261**, 583–612, (2003).

3. Gomar, A., Léonard, T. and others (2012). *ANTARES: Python post-processing library, ver 1.4.0, Cerfacs, Toulouse*. [Online.] available: `http://cerfacs.fr/antares/`.

4. (2012). *ELSA software package, ver 3.4, Onera*. [Online.] available: `http://elsa.onera.fr/index.html`.

5. Bogey, C. and Bailly, C., Computation of a high Reynolds number jet and its radiated noise using Large Eddy Simulation based on explicit filtering, *Computers and Fluids*, **35**, 1344–1358, (2006).

6. Lighthill, M. J., On sound generated aerodynamically: I. General theory, *Proceeding of the Royal Society of London*, **A211**, 564–578, (1952).

7. Ffowcs Williams, J. E. and Hawkings, D. L., Sound generation by turbulence and surfaces in arbitrary motion, *Philosophical Transactions of the Royal Society of London. Series A, Mathematical and Physical Sciences*, **264**, 321–342, (1969).

8. Brentner, K. S. and Farassat, F., Analytical comparison of the acoustic analogy and Kirchhoff formulation for moving surfaces, *American Institute of Aeronautics and Astronautics Journal*, **36**, 1379–1386, (1998).

9. Farassat, F., Derivation of formulations 1 and 1A of Farassat, NASA Technical Memorandum 214853, (2007).

10. Farassat, F., Theory of noise generation from moving bodies with an application to helicopter rotor, NASA Technical Report R-451, (1975).

11. Bogey, C. and Bailly, C., Effects of inflow conditions and forcing on subsonic jet flows and noise, *American Institute of Aeronautics and Astronautics Journal*, **43** (5), 1000–1007, (2005).